Isı Bilimi ve Tekniği Dergisi - Journal of Thermal Science and Technology 45:1 (2025) 22-35

Journal Homepage: https://dergipark.org.tr/tr/pub/isibted

Isı Bilimi ve Tekniği Dergisi

Archive: https://tibtd.org.tr/dergi

Effect of Infrarenal Flow Waveform on Hemodynamics of Abdominal Aortic Aneurysms and Selection of Rheology Models

Burcu RAMAZANLI [1], *, Cüneyt SERT [2], Mehmet Metin Yavuz [2]

[1] *ADA University, School of IT and Engineering, Baku, AZ1008, Azerbaijan*
[2] *Middle East Technical University, Mechanical Engineering Department, Çankaya, 06800, Ankara, Türkiye*

ARTICLE INFO

2025, vol. 45, no.1, pp. 22-35
©2025 TIBTD Online.
doi: 10.47480/isibted.1499633

Research Article
Received: 14 June 2024
Accepted: 08 December 2024

* *Corresponding Author*
e-mail: bramazanli@ada.edu.az

Keywords:
Abdominal aortic aneurysm hemodynamics
Wall shear stress (WSS) descriptors
Vortex transport
Blood rheology
Oldroyd-B model

ORCID Numbers in author order:
0000-0002-8864-7225
0000-0001-7510-9367
0000-0002-9491-4115

ABSTRACT

The infrarenal flow waveform (IFW) demonstrates distinct patterns in response to varying cardiac conditions, raising questions regarding the applicability of the Newtonian model due to variations of the shear rate ($|\dot{\gamma}|$) distribution across different IFW patterns. This study aims to investigate the hemodynamic conditions generated by different IFW patterns within an Abdominal Aortic Aneurysm (AAA) model, and the impact of various rheological models on their predictions. Three IFW patterns are applied to the Newtonian, several shear-thinning and viscoelastic (Oldroyd-B) models. The results of numerical simulations demonstrate the transportation time of the vortices from proximal to distal regions within the bulge decreases by up to 50% with an increase in the mean flow rate. These alterations in the vortex transport mechanism (VTM) affect $|\dot{\gamma}|$ distribution, causing significant variations in the predictions of the rheological models. Even at high mean flow rates, the Newtonian predicts an OSI_{max} twice as large as that predicted by the Carreau and Power models, along with an ECAP_{max} that is 5 times greater. Therefore, the Newtonian model is not appropriate for the AAA simulations. Together with $|\dot{\gamma}|$, a comprehensive assessment of IFW pattern and resulting VTM prior to the rheological model selection is critical and recommended.

İnfrarenal Akış Dalga Formunun Abdominal Aort Anevrizmalarının Hemodinamiği ve Reoloji Modellerinin Seçimi Üzerindeki Etkisi

MAKALE BİLGİSİ

Anahtar Kelimeler:
Abdominal aort anevrizması hemodinamiği
Duvar kayma gerilimi (WSS) tanımlayıcıları
Girdap taşınması
Kan reolojisi
Oldroyd-B modeli

ÖZET

İnfrarenal akış dalga formu (IFW), farklı kardiyak koşullara yanıt olarak belirgin paternler sergilemektedir. Newtonyen modelin Abdominal Aort Anevrizması (AAA) hemodinamiği simülasyonlarında kullanılabilirliği, farklı IFW paternleri arasında kayma hızı ($|\dot{\gamma}|$) dağılımındaki değişiklikler nedeniyle soru işaretleri doğurmaktadır. Bu çalışma, bir AAA modeli içinde farklı IFW paternleri tarafından oluşturulan hemodinamik koşulları ve bu paternlerin çeşitli reolojik modellerin tahminlerine olan etkilerini araştırmayı amaçlamaktadır. Newtonyen, çeşitli kayma inceltici ve viskoelastik (Oldroyd-B) modellerine üç farklı IFW deseni uygulanmıştır. Sayısal simülasyonların sonuçları, anevrizma içinde proksimalden distal bölgelere doğru girdapların taşıma süresinin ortalama akış hızındaki artışla birlikte %50'ye kadar azaldığını göstermektedir. Girdap taşınma mekanizmasındaki (VTM) bu değişiklikler, $|\dot{\gamma}|$ dağılımını etkileyerek reolojik modellerin tahminlerinde önemli varyasyonlara yol açmaktadır. Yüksek ortalama akış hızlarında bile, Newtonyen model, Carreau ve Power modelleri tarafından tahmin edilenden iki kat daha büyük bir OSI_{max} ve beş kat daha büyük bir ECAP_{max} öngörmektedir. Bu nedenle, Newtonyen model, AAA simülasyonları için uygun değildir denilebilir. Sonuç olarak, $|\dot{\gamma}|$'nin yanı sıra, reolojik model seçimi öncesinde IFW paternlerinin ve buna bağlı VTM'nin kapsamlı bir şekilde değerlendirilmesi kritik ve önerilmektedir.

©2025 TIBTD. ISSN 1300-3615 / e-ISSN 2667-7725

SEMBOLLER / NOMENCLATURE

AAA	abdominal aortic aneurysm	λ_{ci}	λ_{ci}-criterion, swirling strength [1/s]
IFW	infrarenal flow waveform	$\overline{\lambda_{ci}}$	time – averaged λ_{ci}-criterion [1/s]
WSS	wall shear stress (Pa)	$\dot{\gamma}$	shear rate (1/s)
TAWSS	time-averaged wall shear stress (Pa)	$\bar{\dot{\gamma}}$	time-averaged shear rate (1/s)
ECAP	endothelial cell activation potential (1/Pa)	α	Womersley number
OSI	oscillatory shear index	ν	kinematic viscosity (m^2/s)
Re_m	mean Reynolds number	μ	dynamic viscosity (Pa.s)

INTRODUCTION

Abdominal aortic aneurysm (AAA) is the dilatation of the abdominal aorta beyond 50% of the normal vessel diameter, due to degeneration of the arterial wall (McGloughlin and Doyle, 2010). The physiological flow waveform at the infrarenal section of the aorta, which is just upstream part of AAA, shows different patterns in different patients. Figure 1 shows measured infrarenal flow waveforms (IFW) for the resting condition of two different patients (Les et al., 2010). There is a significant variation between the peak systolic flow rate values, while the diastolic flow rate is nearly zero for both. However, for exercise conditions, the diastolic flow rate might be higher than zero. According to Les et al. (2010), the diastolic flow rate might reach up to 100 ml/sec during exercise. The variations in the IFW pattern might lead to differences in the hemodynamic conditions such as $|\dot{\gamma}|$ distributions and evolution of the vortex structures through AAAs during systolic and diastolic phases (Fuchs et al., 2021).

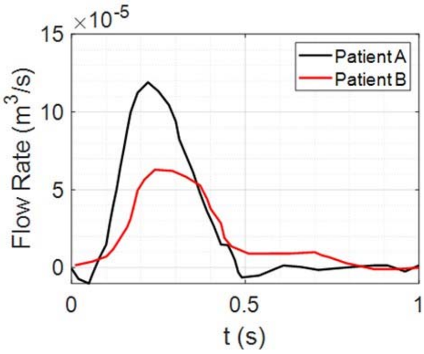

Figure 1. A comparison of measured physiological infrarenal flow rate during rest for two different patients (Les et al., 2010).

Blood is a concentrated suspension of various cellular elements, which are red blood cells, white blood cells and thrombocytes, within the plasma. Plasma, containing 93% water and 3% particles composed of organic molecules, electrolytes, proteins, and waste materials collected from the organism, behaves as a Newtonian fluid with a constant viscosity (Bessonov et al., 2016). However, at low $|\dot{\gamma}|$, especially $|\dot{\gamma}| < 100\ s^{-1}$, the non-Newtonian behavior of blood becomes more apparent. Red blood cells aggregate and form rouleaux, which are rod shaped stacks of individual cells (Bessonov et al., 2016). The aggregation and disaggregation of rouleaux results in a shear-thinning and elastic behavior of blood (Bessonov et al., 2016; Bilgi and Atalik, 2020; Bodnár et al., 2011). The abdominal aorta is a large artery with a high shear rate ($|\dot{\gamma}|$) distribution because the mean flow rate is also larger compared to other arteries (Salman et al., 2019). In literature, it is a common approach to assume the blood as a Newtonian fluid for the hemodynamic simulations of AAAs (Salman et al., 2019; Arzani and Shadden, 2016; Qiu et al., 2018; Soudah et al., 2013) because a vast number of studies agree that non-Newtonian effects diminish with increasing flow rate (Shibeshi and Collins, 2005; Soulis et al., 2008; Skiadopoulos et al., 2017), which leads to a high $|\dot{\gamma}|$ distribution. Indeed, inside the aneurysm sac, there are stagnant low-velocity recirculation regions due to the separation of bulk flow at the diastolic phase (Salman et al., 2019; Arzani, 2018), causing low $|\dot{\gamma}|$ at those zones. Non-Newtonian properties of blood might be more influential during diastole due to lower flow and shear rates (Fisher and Rossmann, 2009), compared to the peak systole. Moreover, aforementioned variations in the IFW pattern might lead different $|\dot{\gamma}|$ distributions through AAAs during the systolic and diastolic phases. Therefore, applicability of the Newtonian model to AAA hemodynamics under various physiological flow conditions remains uncertain.

In numerical studies, shear-thinning behavior of the blood is generally modeled by using various viscosity models, such as Carreau, Carreau-Yasuda, Cross, Casson, Quemada and Power-law. To evaluate differences between the shear-thinning and Newtonian viscosity models, studies have compared hemodynamic descriptors obtained by different shear-thinning models in the cerebral (Fisher and Rossmann, 2009), carotid (Razavi et al., 2011; Morbiducci et al., 2011; Lee and Steinman, 2007; Mendieta et al., 2020) and thoracic (Karimi et al., 2014; Faraji et al., 2022) arteries. For AAAs, several studies (Arzani, 2018; Biasetti et al., 2011; Bilgi and Atalik, 2019) have compared the hemodynamic predictions obtained by the Carreau-Yasuda and Newtonian models, while (Skiadopoulos et al., 2017) compared the results of the Casson, Quemada and Newtonian models. Most of these studies have reported variations between the results obtained with the Newtonian and shear-thinning models. The elastic nature of the blood is commonly modeled by using the Oldroyd-B model (Bodnár et al., 2011). Elhanafy et al. (2019) compared the results obtained by the Newtonian model with the results of viscoelastic Oldroyd-B for AAA, while Bilgi and Atalik (2020) compared the Newtonian, Carreau-Yasuda and modified Oldroyd-B models. However, to the authors' best knowledge, none of the available literature has parametrized the behavior of shear-thinning and viscoelastic rheology models under different hemodynamic conditions which are generated due to varying IFW patterns.

The objective of this study is to investigate the hemodynamic conditions generated by different IFW patterns and their impact on the predictions of a broad range of rheological models including the Newtonian, Carreau, Carreau-Yasuda, Casson, Power, Quemada, Cross, Modified and Simplified Cross, and Oldroyd-B models. For that purpose, three IFW patterns with different peak systolic and diastolic flow rates, which are the Base, Case 1 and 2, are utilized. In literature (Mutlu et al., 2023; Stergiou et al., 2019), hemodynamics of AAA is generally quantified by using WSS descriptors such as time-averaged wall shear stress (TAWSS), oscillatory shear index (OSI), endothelial cell activation potential (ECAP) and relative residence time (RRT). However, WSS descriptors solely are not enough to bridge hemodynamics and aneurysm pathology because vortex patterns are also observed in AAAs (Saqr et al., 2020; Saha et al., 2024). Fuchs et al. (2021) observed the effect of IFW pattern on aorta hemodynamics, and their results highlighted a substantial impact of the IFW pattern on WSS descriptors. Moreover, they also revealed strong variations in vortex structures, but this aspect is not fully explored in the scope of their study. Hence, they recommend further investigation to understand the impact of IFW pattern on vortex evolution (Fuchs et al., 2021). Moreover, in a meta literature analysis study, Saqr et al. (2020) have reported that WSS is a scalar-tensor field, which loses its directionality. Visualizing vortex patterns rather than WSS descriptors is more meaningful owing to their directional nature. Therefore, together with WSS descriptors, quantifying the vortical structures and their evolution may lead to better understanding the effect of IFW both on AAA hemodynamics and predictions of various rheology models (Saqr et al., 2020; Saha et al., 2024).

METHODS

In their patient-specific aorta study, Fuchs et al. (2021) emphasized that variations in the IFW pattern considerably affect the vortex structures. However, they also highlighted that in the context of patient-specific geometries, the flow field becomes extremely complex, making it impractical to accurately parametrize the effect of IFW pattern on vortex structures (Fuchs et al., 2021). In this study, an idealized model of AAA is employed, chosen for its suitability for a comparative parametric study. Owing to its independence from geometric details, the use of an idealized geometry is advantageous for characterizing and comparing predictions of a broad range of rheology models according to different hemodynamic conditions under various IFW patterns. The AAA model used in this study is given in Fig. 2a. The geometry is two-dimensional, axisymmetric, and created based on Stamatopoulos et. al's study (2010). The entrance and exit parts are straight and cylindrical, while the aneurysm bulge is elliptical with a major radius of 0.034 m. The lengths of the entrance part, bulge and exit parts are $L_{ent} = 935$ mm, $L_B = 62$ mm and $L_{ex} = 206$ mm, respectively. The artery and bulge radii are, $R = 9$ mm and $R_B = 22$ mm, respectively. The vessel and bulge dimensions are consistent with those of realistic abdominal arteries and aneurysms (Brewster et al., 2003; Les et al., 2010).

Figure 2b shows the IFW patterns used at the inlet, which are the Base, Case 1, and Case 2. In the Base case, the IFW pattern suggested by Finol and Amon is implemented, by preserving the overall waveform characteristics. However, the peak flow rate suggested by Finol and Amon (2001) is lower than the physiologically measured values (Suh et al., 2011). To align with the physiological range, the peak flow rate in the Base case is adjusted upward to reach a peak systolic flow rate of 42 ml/sec, starting from a diastolic flow rate of zero. It is important to note that, while IFW pattern is derived from the Finol and Amon's study (2001), there is no direct comparison between their results and the results of this study. Consequently, the results are not affected by the difference in the peak flow rates between the two studies. In Case 1, the diastolic flow rate remains consistent with that of the Base case, while the peak systolic flow rate is increased. On the other hand, in Case 2 the amplitude of peak systole is kept identical to that of the Base pattern, albeit with increased diastolic flow rate. Therefore, Cases 1 and 2 serve to investigate the impact of increased peak systolic and diastolic flow rates, respectively. The period of all waveforms is the same and equal to $T = 1$ s, yielding a Womersley number of $\alpha = 0.5D\sqrt{\omega/\nu} = 12.14$, where D is the artery diameter, $\omega = 2\pi/T$ is the frequency, and $\nu = 3.45 \times 10^{-6}$ m^2/s is the kinematic viscosity of the Newtonian model. The mean Reynolds numbers for the waveforms are $Re_m = U_m D/\nu = 120, 250$ and 1160, where $U_\mathrm{m} = 0.023, 0.048$ and 0.223 m/s are the time averaged velocities over one period for the Base, Case 1 and 2, respectively.

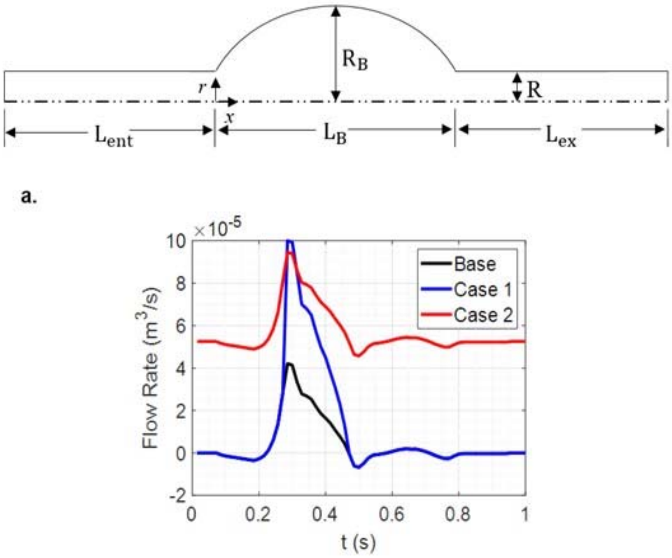

Figure 2. a. 2D axisymmetric flow domain (out of scale). Flow is from left to right, **b.** Physiological IFW patterns, Base (Finol and Amon, 2001), Case 1 and 2.

Unsteady plug flow is specified at the inlet. To capture the transient effects of physiological flow, a Womersley profile at the inlet is generally recommended (Madhavan and Kemmerling, 2018; Moyle et al., 2006; Ramazanli et al., 2023, Wei et al., 2019; Womersley, 1955). The preliminary analysis (Ramazanli et al., 2023) found that while a minimum entrance length of 10D is sufficient for fully developing Womersley flow, a longer entrance length (50D) was applied in this study to achieve consistency across different IFW cases and to ensure a fully developed profile at the bulge inlet. A constant reference pressure of 0 Pa is specified at the outlet, which is a frequently utilized approach in the literature for hemodynamic studies (Reza and Arzani, 2019; Soulis et al., 2008). Through the preliminary runs, it is ensured that the length of the exit part is long enough that the disturbance created by the bulge dies out before the flow reaches the outlet, enabling the use of constant pressure outlet.

The wall boundaries are taken as rigid with no-slip boundary conditions applied. Excluding the compliance effect by using rigid walls is quite common in literature (Arzani and Shadden, 2016; Finol and Amon, 2001; Reza and Arzani, 2019). Eight non-Newtonian models, Carreau, Carreau-Yasuda, Casson, Quemada, Power, Cross, Simplified and Modified Cross, with the details given in Table 1, are used. For the Power model, different constants are available in literature for the same hematocrit.

Table 1. Selected shear-thinning rheology models, which are frequently used to model blood (Bessonov et al., 2016; Shibeshi and Collins, 2005; Cho and Kensey, 1991; Quemada, 1978; Stergiou et al., 2019).

Carreau	$\frac{\mu(\dot{\gamma}) - \mu_\infty}{\mu_0 - \mu_\infty} = (1 + (\lambda\dot{\gamma})^2)^{(n-1)/2}$	$\mu_0 = 0.056\ \mathrm{Pa \cdot s}$ $\mu_\infty = 0.00345\ \mathrm{Pa \cdot s}$ $\lambda = 3.313\ \mathrm{s}$ $n = 0.3568$
Carreau-Yasuda	$\frac{\mu(\dot{\gamma}) - \mu_\infty}{\mu_0 - \mu_\infty} = (1 + (\lambda\dot{\gamma})^a)^{(n-1)/a}$	$\mu_0 = 0.056\ \mathrm{Pa \cdot s}$ $\mu_\infty = 0.00345\ \mathrm{Pa \cdot s}$ $\lambda = 1.902\ \mathrm{s}$ $n = 0.22$ $a = 1.25$
Quemada	$\mu = \mu_f \left[1 - \frac{1}{2} \frac{K_0 + K_\infty \sqrt{\frac{\lvert\dot{\gamma}\rvert}{\gamma_c}}}{1 + \sqrt{\frac{\lvert\dot{\gamma}\rvert}{\gamma_c}}} \phi \right]$	$\mu_f = 0.0012\ \mathrm{Pa \cdot s}$ $K_0 = 4.65$ $K_\infty = 1.84$ $\gamma_c = 2.23\ \mathrm{s}^{-1}$ $\phi = 0.4$
Casson	$\sqrt{\tau} = \sqrt{k_0} + \sqrt{k_1\dot{\gamma}}$	$k_0 = 0.05\ \mathrm{dyne/cm^2}$ $k_1 = 0.04\ \mathrm{dyne/cm^2}$
Cross	$\frac{\mu(\dot{\gamma}) - \mu_\infty}{\mu_0 - \mu_\infty} = \frac{1}{1 + (m\dot{\gamma})^n}$	$\mu_0 = 0.056\ \mathrm{Pa \cdot s}$ $\mu_\infty = 0.00345\ \mathrm{Pa \cdot s}$ $m = 1.007\ \mathrm{s}$ $n = 1.028$
Simplified Cross	$\frac{\mu(\dot{\gamma}) - \mu_\infty}{\mu_0 - \mu_\infty} = \frac{1}{1 + m\dot{\gamma}}$	$\mu_0 = 0.103\ \mathrm{Pa \cdot s}$ $\mu_\infty = 0.005\ \mathrm{Pa \cdot s}$ $m = 8\ \mathrm{s}$
Modified Cross	$\frac{\mu(\dot{\gamma}) - \mu_\infty}{\mu_0 - \mu_\infty} = \frac{1}{(1 + (m\dot{\gamma})^n)^a}$	$\mu_0 = 0.056\ \mathrm{Pa \cdot s}$ $\mu_\infty = 0.00345\ \mathrm{Pa \cdot s}$ $m = 3.736\ \mathrm{s}$ $n = 2.406$ $a = 0.254$
Power	$\mu(\dot{\gamma}) = K\dot{\gamma}^{n-1}$	$K = 0.017\ \mathrm{Pa \cdot s^n}$ $n = 0.708$ (Shibeshi and Collins, 2005) and $K = 0.035\ \mathrm{Pa \cdot s^n}$ $n = 0.6$ (Cho and Kensey, 1991)

In the present study, Power-1 (Shibeshi and Collins, 2005), and Power-2 (Cho and Kensey, 1991) are tested by using two frequently used constants. In Table 1, μ is the viscosity, μ_0 and μ_∞ are the asymptotic viscosity values at zero and infinite shear rates, λ is the relaxation time constant, K is the flow consistency index and n is the power law index (Bessonov et al., 2016; Shibeshi and Collins, 2005; Cho and Kensey, 1991). The kinematic viscosity is $3.45 \times 10^{-6}\ \mathrm{m^2/s}$ for the Newtonian approach, and the density is $1000\ \mathrm{kg/m^3}$ for all models (Bessonov et al., 2016)To account for the elastic nature of blood, the stress tensor in the linear momentum equation can be decomposed into viscous and elastic parts as $\tau = \tau_s + \tau_e$. The viscous part of the Oldroyd-B model is Newtonian, $\tau_s = 2\mu_s(\nabla u + \nabla u^T)$ (Bodnár et al., 2011). The elastic part satisfies the following constitutive equation.

$$\tau_e + \lambda_1 \left(\frac{\partial \tau_e}{\partial t} + u \cdot \nabla\tau_e - \tau_e \cdot \nabla u - \nabla u^T \cdot \tau_e \right) = \mu_e(\nabla u + \nabla u^T) \qquad (1)$$

where μ_e is the elastic viscosity coefficient, and λ_1 is the relaxation time (Leuprecht and Perktold, 2001). For blood, $\mu_e = 0.0004\ \mathrm{Pa \cdot s}$ and $\lambda_1 = 0.06\ \mathrm{s}$ (Leuprecht and Perktold, 2001). The Oldroyd-B model available in OpenFOAM is tested previosly (Habla et al., 2014; Guranov et al., 2013; Javidi et al. 2015).

The maximum number of iterations performed at each time step is taken as 10, and the solutions are considered to be converged when residuals for axial velocity component and pressure are less than 10^{-4}. Time step for all simulations is selected as 10^{-5} sec, and to ensure that the time periodic state is reached, calculations are repeated for 6 cardiac cycles for shear-thinning and Newtonian models. However, 12 cardiac cycles are used to reach the time periodic state for Oldroyd-B model. To select a suitable mesh, a mesh independence study is performed using four structured meshes given in Fig. 3.

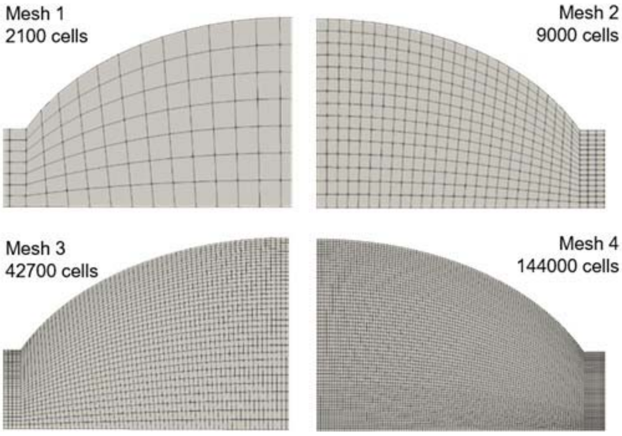

Figure 3. Four meshes used for the mesh independence check.

Figure 4a shows axial velocity profiles at the mid-plane of the aneurysm and swirling strength, λ_{ci} contours obtained at the peak systole and early diastole. In Figure 4b, OSI and ECAP distributions obtained are provided. The axial velocity profiles are identical and swirling strength contours are very similar for meshes 3 and 4. Albeit OSI and ECAP distributions are very sensitive to the mesh selection, Mesh 3 and 4 provided very similar OSI and ECAP distributions. Therefore, Mesh 3 is evaluated to be suitable and used to perform the simulations in the present study.

Stamatopoulos et al. (2010) have performed an experimental and numerical study in axisymmetric bulges similar to the those used in the present study with a steady inlet flow. As a general verification of the currently used simulation setup, axial velocity profiles obtained by Stamatopoulos et al. (2010) are compared with those obtained in the present study with a steady inlet flow in Fig. 5a. The match in the profiles is considered to be satisfactory. Ohtaroglu (2020) performed experiments with physiological, unsteady inlets using Stamatopoulos et al.'s geometry. Figure 5c compares the streamlines obtained in those experiments with the current simulation results at four different time instants of the physiological cycle. Progression of focus points in streamlines, which are the indication of vortex core movement, shows good agreement. Considering both the spatial and the temporal evolution during the cycle, the model predictions are considered to be satisfactory. In addition, simulations are performed to ensure the validity of 2D axisymmetric simplification by comparing results with those of 3D simulations. Considering the velocity profiles plotted at the mid plane of the bulge in Fig. 5c, 2D axisymmetric and 3D results turn out to be almost identical.

WSS descriptors and swirling strength

Generally, wall shear stress (WSS) distribution and different WSS descriptors are used in the literature to predict aneurysm development, thrombosis formation and rupture (Salman et al., 2019; Mutlu et al., 2023). TAWSS descriptor evaluates the total shear stress exerted on the wall throughout a cardiac cycle and OSI highlights zones where WSS shows directional changes over the cardiac cycle (Pinto and Campos, 2016). ECAP and RRT combine TAWSS and OSI in different ways. Mathematical definitions of these descriptors are given below

$$TAWSS = \frac{1}{T}\int_0^T |\tau_w| dt \tag{2}$$

$$OSI = 0.5\left(1 - \frac{\left|\frac{1}{T}\int_0^T \tau_w dt\right|}{\frac{1}{T}\int_0^T |\tau_w| dt}\right) \tag{3}$$

$$ECAP = \frac{OSI}{TAWSS} \tag{4}$$

$$RRT = \frac{1}{(1-2OSI)TAWSS} \tag{5}$$

where T and τ_w are the cardiac cycle period and the wall shear stress, respectively.

Vortex structures are studied extensively in fluid mechanics (Epps, 2017; Chen et al., 2015) because in many cases they provide important insights into the flow field. Inside the aneurysm sac, there is a vortex ring that evolves throughout the cardiac cycle (Bilgi and Atalik, 2019; Deplano et al., 2016). Therefore, together with WSS descriptors, vortex patterns also provide valuable information regarding AAA hemodynamics. Saqr et al. (2020) suggested investigating flow field within aneurysms via vector fields such as vorticity, rather than scalar-tensor fields. However, the vorticity field is not able to discriminate shear layers and vortices (Chen et al., 2015). Swirling strength, λ_{ci}, is a velocity gradient-based vortex identification criteria, which uses discriminant of characteristic equation to define a vortex without shear layers and takes the following form for a 2D axisymmetric flow (Chen et al., 2015)

$$\lambda_{ci} = \frac{1}{2}\sqrt{-4\frac{\partial u_r}{\partial x}\frac{\partial u_x}{\partial r} - \left(\frac{\partial u_x}{\partial x} - \frac{\partial u_r}{\partial r}\right)^2} \tag{6}$$

where u_r and u_x are radial and axial velocity components, respectively. λ_{ci} is larger than zero around a vortex region (Chen et al., 2015).

RESULTS

Effect of IFW pattern on AAA hemodynamics

To understand the hemodynamics of the three IFW patterns inside the AAA model, the temporal evolution of vortex structures, obtained by using the Carreau model, is presented in Supplementary Video 1. For all IFW patterns which are presented as the Base, Case 1 and 2, a primary vortex is generated due to acceleration of the bulk flow during early systole. It is separated from the inlet of the bulge at the peak systole, t = 0.3 sec, and transported downstream by means of advection. The primary phenomena differing from those of the Base, Case 1 and 2 are the acceleration and advection of the bulk flow. For the Base waveform, the acceleration is relatively minor compared to that in Case 1, resulting in only a weaker primary vortex with a small $|\lambda_{ci}|$. Advective effects are also not dominant due to low mean flow rate. Therefore, the primary vortex dissipates due to viscous diffusive effects before it reaches the central region. The largest acceleration is obtained by Case 1. During early systole, the larger acceleration generates a stronger vortex with a large $|\lambda_{ci}|$ compared to the Base case and Case 2. The vortex maintains itself as a strong identity and remains transported to the distal region until the end of the cardiac cycle at $t = T$. On the other hand, increased advective effects due to the larger mean flow rate in Case 2 resulted in the transport of the vortex to the distal site being completed by the end of the systolic phase at $t = 0.5T$. During the diastolic phase, the vortex in Case 2 is located at the distal zone and dissipates due to viscous effects by the end of the cycle, whereas the primary vortex of Case 1 maintains its strong identity even during late diastole.

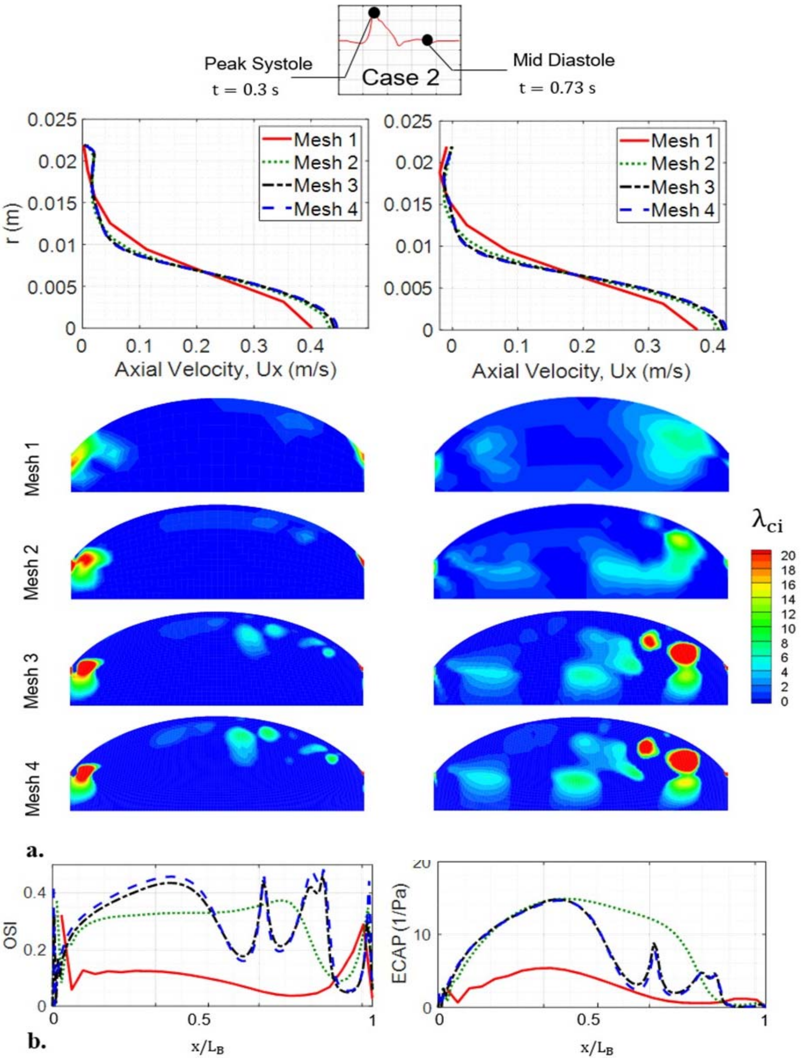

Figure 4. **a.** Axial velocity profiles obtained with four different meshes at the mid-plane of the aneurysm, $x/L_B = 0.5$, and swirling strength contours through the bulge at the peak systole and mid diastole, b. OSI and ECAP distributions of four meshes for Case 2.

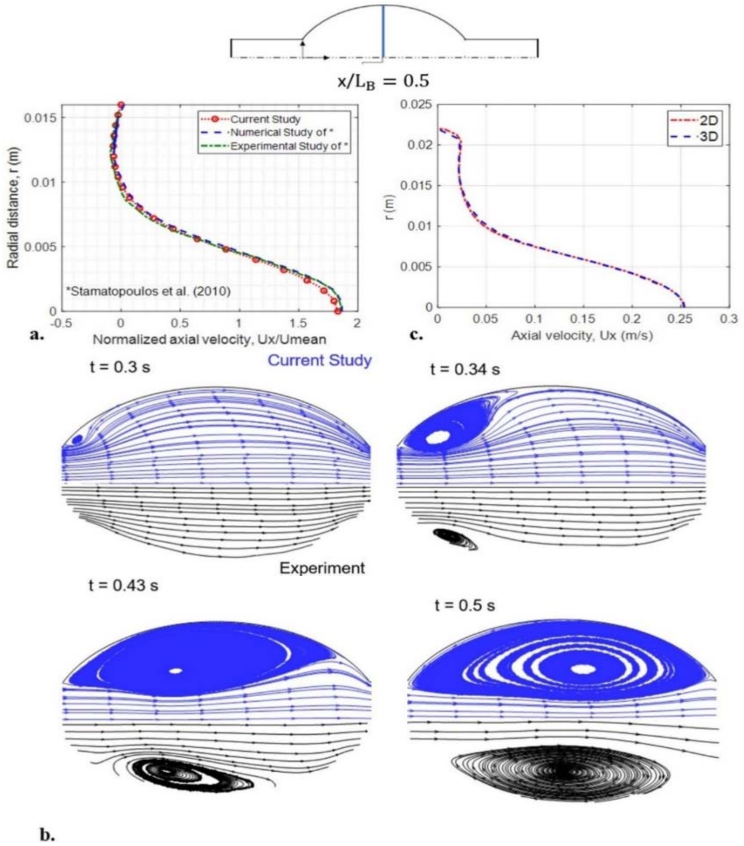

Figure 5. **a**. Comparison of the normalized axial velocity profile of the current study at x/L$_B$=0.5 with results of Stamatopoulos et al. (2010) for a steady inlet velocity, **b.** Comparison of the streamline patterns of different time instants for a cardiac cycle; upper halves show the current results and lower halves are from Ohtaroglu (2020), c. Comparison of the axial velocity profiles of 2D axisymmetric and 3D geometries at x/L$_B$=0.5 at t=0.3 sec of Base case.

Figure 6 presents the contours of the time-averaged swirling strength, $\overline{\lambda_{ci}}$, streamlines and variations in WSS descriptors for three IFW patterns. The Base pattern generates a single primary vortex pattern, in the proximal region of the bulge. However, for Cases 1 and 2, a second primary and a secondary vortex are also generated, and the primary vortex is located in the distal region with a larger magnitude of $\overline{\lambda_{ci}}$ than in the Base case. For Case 1, the second primary and secondary vortices are in the proximal and central regions, respectively. However, for Case 2, they are both located in the distal zone, in contrast to the Base case. As illustrated in Fig. 6, there is a strong correlation between WSS descriptors and vortex patterns. TAWSS obtains high values around the vortices, particularly in large $|\overline{\lambda_{ci}}|$ zones in proximity to the wall, where the OSI, ECAP and RRT are low. For all the cases magnitudes of the ECAP and RRT become zero with high $|\overline{\lambda_{ci}}|$ in the regions where the primary vortex is located. However, the ECAP and RRT values increase significantly in regions with high stagnation. $\mathrm{ECAP_{max}}$ and $\mathrm{RRT_{max}}$ for the Base case are three times larger than those of Case 1, which has low stagnancy.

Effect of the IFW pattern on predictions of the rheology models

To investigate the effect of the IFW pattern on the behavior of rheology models, instantaneous WSS distributions, contours of swirling strength, λ_{ci}, and shear rate, $\dot{\gamma}$, are plotted in Fig. 7. In the literature, the most significant deviations between the Newtonian and shear-thinning models are observed at the diastolic phase due to the low flow rate (Shibeshi and Collins, 2005), which is consistent with the results of the present study. The mid-diastolic phase (Egelhoff et al., 1999) was selected as it corresponds to the lowest shear rates, where non-Newtonian blood behavior becomes more significant. To provide a comprehensive investigation of hemodynamics, Supplementary Material includes figures and videos showing the evolution of swirling strength throughout the entire cardiac cycle, covering all diastolic phases for each IFW case. Therefore, the results of mid diastolic phase, t = 0.73 sec, are presented in Fig. 7. In Case 1, $|\dot{\gamma}|$ remains low for most of the bulge, while $|\dot{\gamma}| > 50\ \mathrm{s^{-1}}$ around the primary vortex. Compared to shear-thinning models, the Newtonian model overestimates the WSS peak, intensity of swirling strength contours and $|\dot{\gamma}|$, which is consistent with literature (Biasetti et al., 2011). The WSS distributions, patterns of λ_{ci} contours and their locations are very similar for the Casson and Quemada models, consistent with the results of (Skiadopoulos et al., 2017). The Carreau and Power models predict comparable λ_{ci} patterns and WSS distributions, as reported by (Shibeshi and Collins, 2005). Although not presented here, the Carreau-Yasuda, Cross, Modified and Simplified Cross models are also tested. The results obtained by the Carreau-Yasuda, Cross and Modified Cross are the same with Carreau and Power-1, while the Simplified Cross model provided very similar hemodynamic descriptors with the Casson and Quemada for all cases. For Case 2, $|\dot{\gamma}| > 50\ \mathrm{s^{-1}}$ is obtained near the distal region and at the centerline of the aneurysm, while it remains close to zero in proximity to the wall for proximal and central regions. At regions with high $|\dot{\gamma}|$, contours of λ_{ci} and WSS distribution obtained by the Carreau, Carreau-Yasuda, Cross, Modified and Simplified Cross, Casson, Quemada and Newtonian models are very similar to each other. Therefore, the Newtonian model might be sufficient for the zones with $|\dot{\gamma}| > 50\ \mathrm{s^{-1}}$, while the shear-thinning models are necessary for the stagnant regions with significantly lower shear rates.

In Supplementary Figure, the WSS distributions, λ_{ci} and $|\dot{\gamma}|$ contours of peak systolic phase, t = 0.3 sec, are presented at the post-bulge, straight artery segment for Case 1 and 2. In this specific region, near-wall $|\dot{\gamma}|$ values exhibit a significant increase compared to the values in proximity to the bulge. The results demonstrate that, the Casson and Quemada models demonstrate a diverging behavior from the Newtonian model as $|\dot{\gamma}|$ values are increasing, whereas the Carreau and Power models exhibit a more consistent behavior. It is the fact that for large $|\dot{\gamma}|$ values ($|\dot{\gamma}| > 100\ \mathrm{s^{-1}}$), blood demonstrates Newtonian characteristics (Bessonov et al., 2016), the suitability of Casson and Quemada models in modeling the rheological behavior of blood might be questionable, particularly in scenarios characterized by elevated $|\dot{\gamma}|$ values.

Figure 8 shows contours of time-averaged swirling strength, $\overline{\lambda_{ci}}$, shear rate, $\bar{\dot{\gamma}}$, and streamlines obtained by the Carreau, Power, Casson, Quemada and Newtonian models for Base, Case 1 and 2. For the Base case, $|\bar{\dot{\gamma}}| < 10\ \mathrm{s^{-1}}$ throughout the bulge, and the Newtonian model overestimates the magnitude and intensity of $\overline{\lambda_{ci}}$ contours of vortices. From the $\overline{\lambda_{ci}}$ contours, non-Newtonian behavior in low shear zones minimizes the size of the primary vortex pattern for all of the shear-thinning models (Soulis et al., 2008), and a second primary vortex is only obtained by the Newtonian model.

For Case 1, $|\bar{\dot{\gamma}}|$ is larger than $50\ \mathrm{s^{-1}}$ only around the primary vortex, but it is nearly zero at other regions. $\overline{\lambda_{ci}}$ contours and streamline patterns of the Newtonian model are significantly different than the other rheology models. On the other hand, except the proximal and central regions, $|\bar{\dot{\gamma}}| > 50\ \mathrm{s^{-1}}$ inside the bulge for Case 2. Therefore, $\overline{\lambda_{ci}}$ and streamline predictions of all shear-thinning models become very similar to the Newtonian model. With increasing shear rate, except the Power-2, all rheology models can predict the primary, second primary and secondary vortices. Biasetti et al. (2011) have reported that the Newtonian model predicted vortex structures at the core region, away from the near wall, which were not observed with the more accurate Carreau–Yasuda model. Moreover, Arzani (2016) has hypothesized that shear-thinning models predict different vortex patterns than the Newtonian model. The present study further supports those hypotheses quantitatively, revealing that the Newtonian model especially tends to overestimate the magnitude and intensity of $\overline{\lambda_{ci}}$ contours of secondary and second primary vortices.

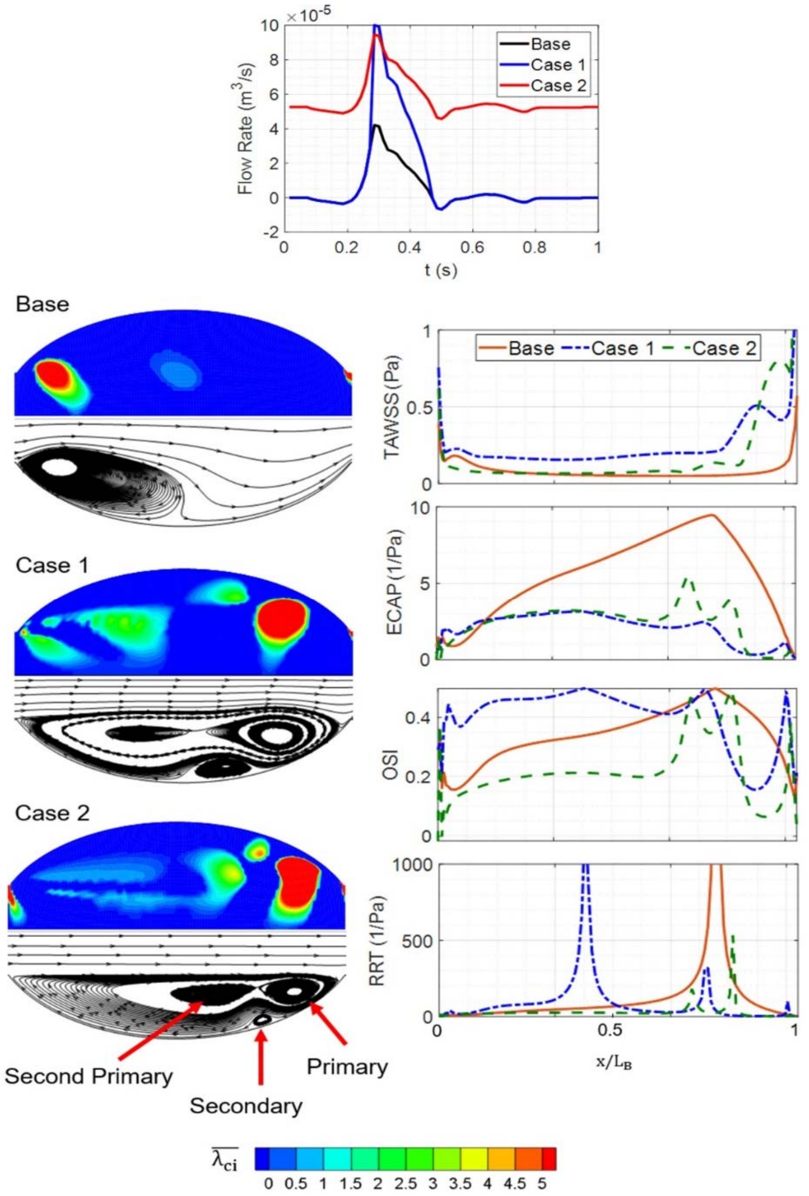

Figure 6. Comparison of time-averaged swirl strength contours, streamlines and variations in WSS measures on the aneurysm wall for the Carreau model for three IFW patterns

In Figure 9, OSI and ECAP distributions obtained by selected rheology models are presented. As observed in Fig. 6, OSI and ECAP values are near to zero around high $|\overline{\lambda_{ci}}|$ region, while they tend to increase for decreasing $|\overline{\lambda_{ci}}|$ for each waveform and rheology model. OSI and ECAP distributions obtained by the Casson and Quemada models are nearly the same, and closer to the Newtonian pattern at each waveform, consistent with the results of Fig. 8. OSI and ECAP estimations of the Carreau and Power-1 models are very similar and more dissipative than the Casson and Quemada, which is an expected behavior for a shear-thinning model (Biasetti et al., 2011). Power-2 is significantly dissipative and its OSI and ECAP patterns are very different than other shear-thinning models. Even for Case 1 and 2, with comparatively higher $|\bar{\dot{\gamma}}|$ values inside the bulge, the Newtonian model overestimates the OSI and ECAP values. Especially for Case 2 with the highest mean flow rate, OSI and ECAP values obtained by the Newtonian model are significantly larger for the proximal and central regions of the bulge ($0 < x/L_B < 0.65$) than the shear-thinning models, although they obtain quite similar $\overline{\lambda_{ci}}$ patterns as seen in Fig. 8.

OSI and ECAP estimations of the Carreau and Power-1 models are very similar and more dissipative than the Casson and Quemada, which is an expected behavior for a shear-thinning model (Biasetti et al., 2011). Power-2 is significantly dissipative and its OSI and ECAP patterns are very different than other shear-thinning models. Even for Case 1 and 2, with comparatively higher $|\bar{\dot{\gamma}}|$ values inside the bulge, the Newtonian model overestimates the OSI and ECAP values. Especially for Case 2 with the highest mean flow rate, OSI and ECAP values obtained by the Newtonian model are significantly larger for the proximal and central regions of the bulge ($0 < x/L_B < 0.65$) than the shear-thinning models, although they obtain quite similar $\overline{\lambda_{ci}}$ patterns as seen in Fig. 8.

OSI$_{max}$ value obtained by the Newtonian model at that segment is 2 times larger than the Carreau and Power, while 1.5 times larger than Casson and Quemada models. ECAP$_{max}$ value of the Newtonian at that zone is 5 and 2.5 times larger than Carreau-Power and Casson-Quemada pairs, respectively.

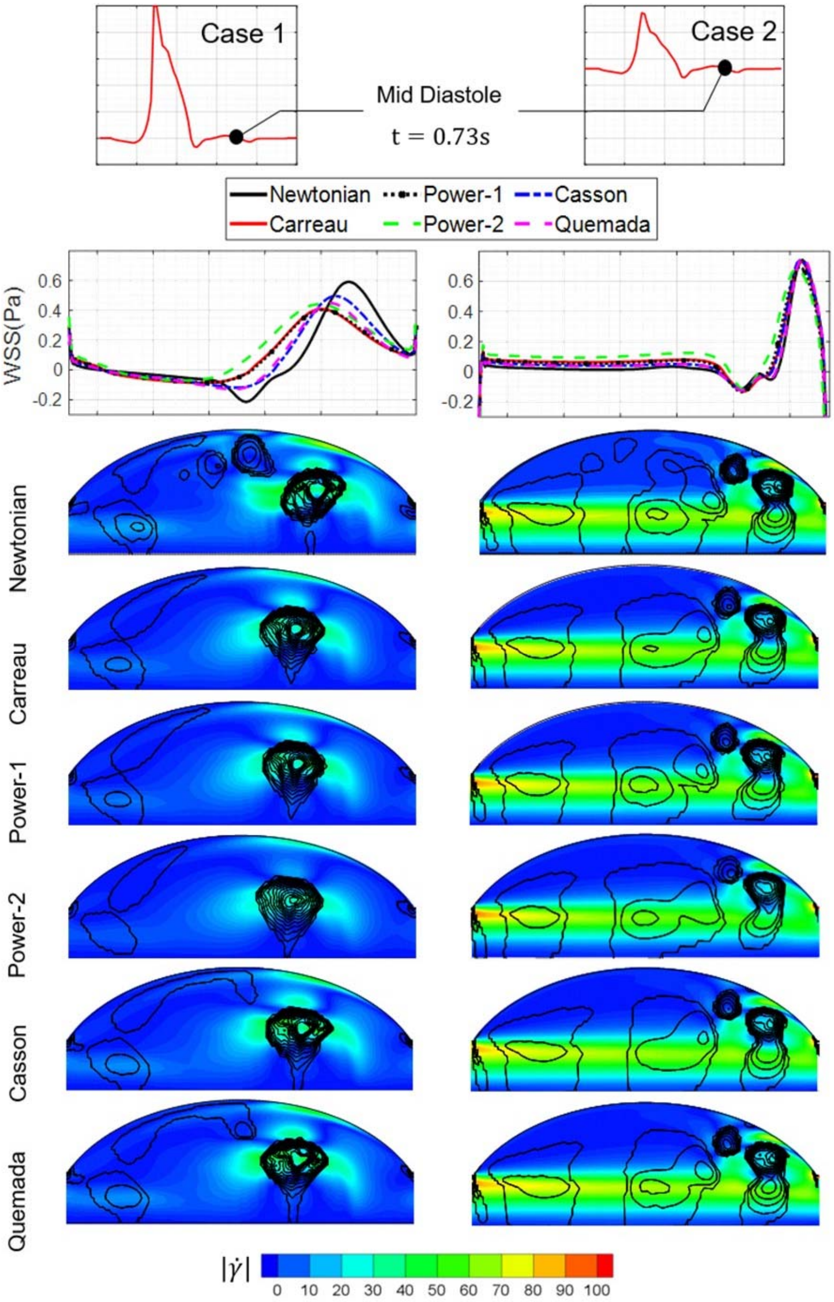

Figure 7. Comparison of WSS distributions, λ_{ci} and $|\dot{\gamma}|$ contours of Newtonian and selected shear-thinning rheology models at t = 0.73 sec, for cases 1 and 2.

Differences of the hemodynamic predictions of the Newtonian, shear-thinning and Viscoelastic models

To the author's best knowledge, this is the first study which utilizes Oldroyd-B model of OpenFOAM to simulate hemodynamics of an AAA model. Base case is selected here because the Oldroyd-B model available in OpenFOAM fails to provide a stable solution for high mean Reynolds numbers, such as Case 1 and 2. This observation is consistent with literature, where multiple studies have documented the inadequacies of the Oldroyd-B model in accurately capturing flow dynamics of high Reynolds numbers (Elhanafy et al., 2019; Leuprecht and Perktold, 2001). Indeed, the elasticity of blood is dominant for low shear rates, demonstrating a diminishing pattern with increasing shear rate ($|\dot{\gamma}| > 100\ s^{-1}$) (Bodnár et al., 2011). Therefore, comparing the results of the Newtonian, Viscoelastic, Quemada and Carreau models for the Base case with lower shear provides insights into the differences introduced by blood elasticity.

In Figure 10a, λ_{ci} contours and streamline patterns for the Base case are presented for the Newtonian, Viscoelastic, Quemada and Carreau models at the mid-diastolic phase (t = 0.73 sec). The selection of the Base case is motivated by its characteristic low shear rates. The viscous part of the Viscoelastic Oldroyd-B model is Newtonian, not shear-thinning. On the other hand, the Carreau and Quemada models are shear-thinning models and could only provide viscous behavior. Therefore, the difference between the Newtonian and Viscoelastic results is caused by the elastic effects, while the shear-thinning models and Newtonian case present variations caused only by viscous effects.

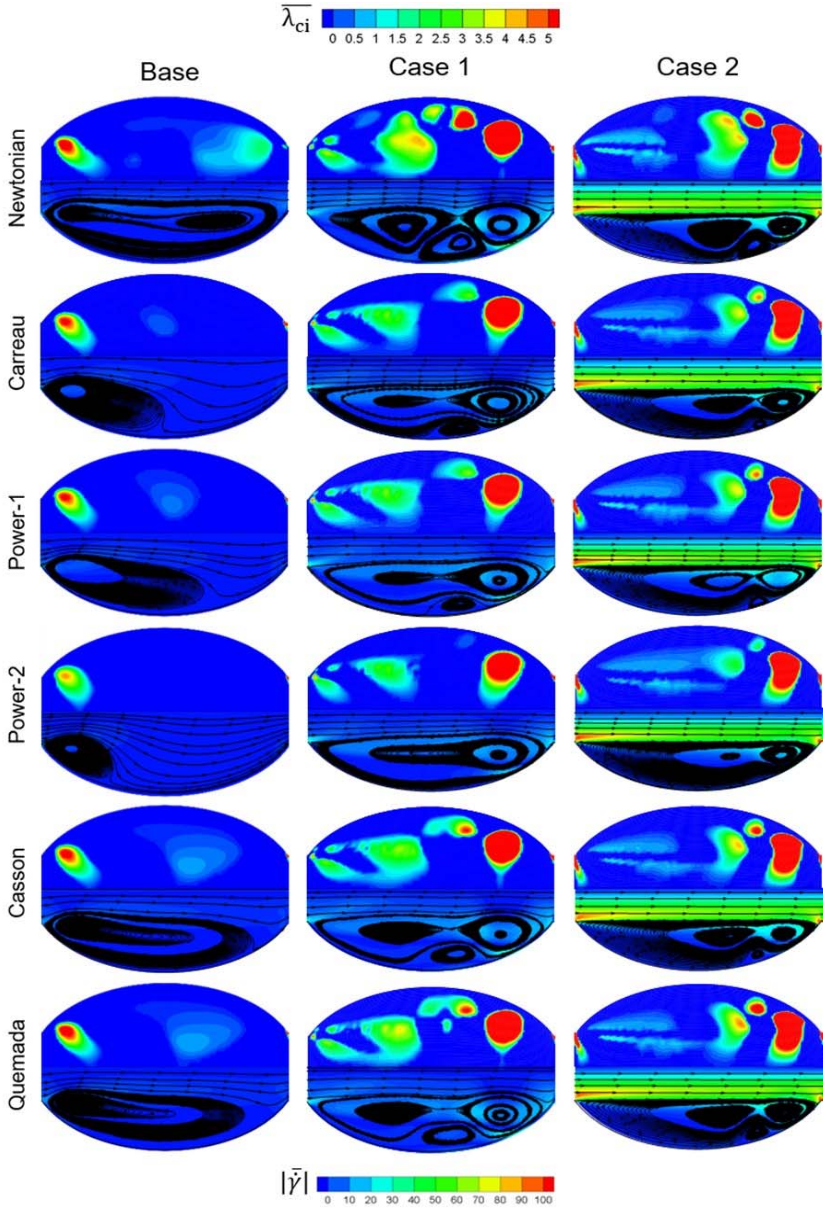

Figure 8. Comparison of time-averaged streamline patterns, $\overline{\lambda_{ci}}$ (upper parts) and $|\bar{\dot{\gamma}}|$ contours (bottom parts) of selected rheology models

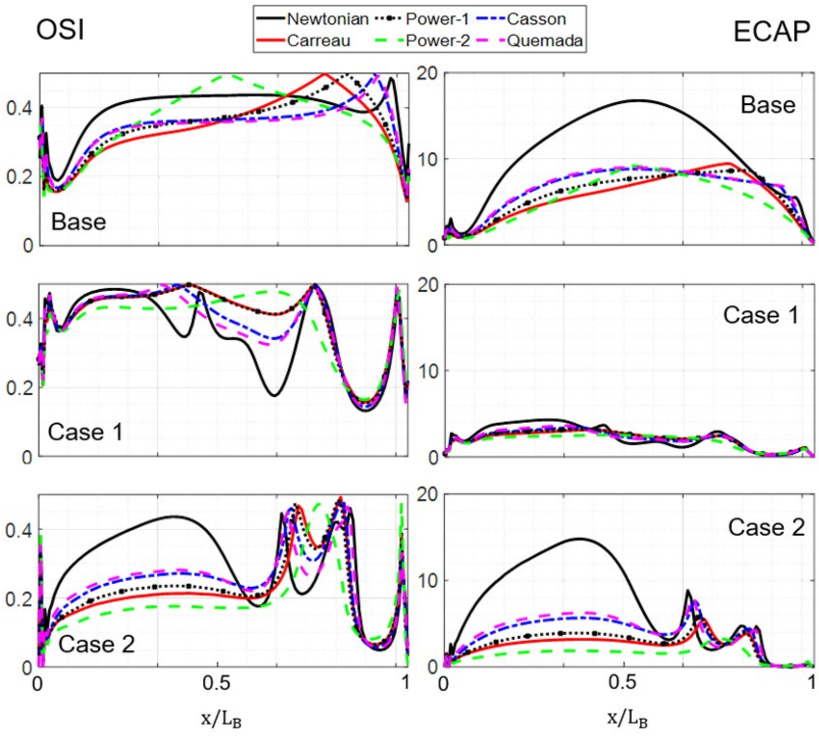

Figure 9. Comparison of OSI and ECAP distribution on the aneurysm wall of selected rheology models.

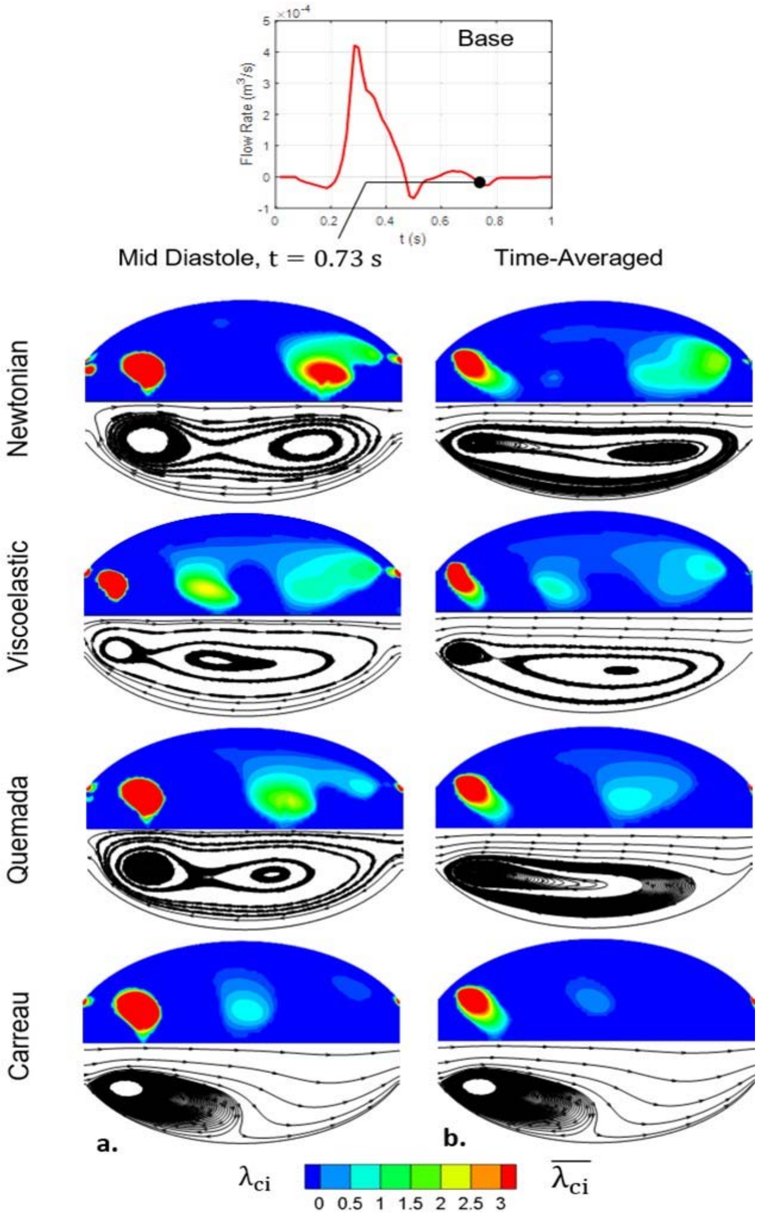

Figure 10. Comparison of a. λ_{ci} contours and instantaneous streamline patterns at t = 0.73 sec, b. $\overline{\lambda_{ci}}$ contours and time-averaged streamline patterns of selected models for the Base case.

Compared to other models, the size of primary vortex obtained by the Viscoelastic model is smaller and it is located in closer proximity to the inlet of the bulge. From the streamlines and contours of λ_{ci}, a second primary vortex is observed for the Newtonian, Viscoelastic and Quemada models, but the core locations are different. The core of the second primary vortex of the Newtonian model is located near to the distal region, while it is located at the central zone for the Viscoelastic and Quemada models. In Fig. 10b, the time-averaged streamline patterns are presented. Location of the time-averaged primary and second primary vortex cores and $\overline{\lambda_{ci}}$ contours obtained by the Viscoelastic model are more similar to the Newtonian model, compared to the Carreau and Quemada models. Aforementioned shear-thinning models do not predict a time-averaged second primary vortex.

DISCUSSION

The current study investigates the impact of infrarenal flow waveform (IFW) patterns on AAA hemodynamics and the behavior of the Newtonian, viscous shear-thinning and viscoelastic rheology models. For that purpose, three IFW patterns, Base, Case 1 and 2, are implemented in a simplified AAA model as the inlet boundary conditions. In comparison to the baseline represented by the Base case, Cases 1 and 2 are specifically designed to assess the impact of increased peak systolic and diastolic flow rates, respectively. Fig. 6 and Supplementary Video-1 clearly demonstrate that the IFW pattern exerts a significant influence on both the vortex structure and WSS descriptors. The primary vortex of the Base case cannot reach the distal region, while its transportation to the distal site is completed by the end of the systolic phase at $t = 0.5T$. On the other hand, the vortex transport for Case 1 persists until the end of one full cardiac cycle, $t = T$, with no fixed settling zone for an extended period. This prolongs the oscillatory nature of the flow pattern, resulting in elevated OSI values. Throughout the bulge, the magnitude of OSI for Case 1 is greater than that for the other waveforms, which might be related to vortex transport. Moreover, regions with large $|\overline{\lambda_{ci}}|$ values exhibit nearly zero OSI, ECAP and RRT values. Hence, both the strength of the vortex and its transportation mechanism (VTM) influence the distribution and magnitude of WSS descriptors.

Fig. 7 reveals that the shear-thinning rheology model is as effective for determining AAA hemodynamics as is the case for IFW patterns. The Newtonian model tends to overestimate the WSS peak, intensity, and magnitude of swirling strength of the vortex patterns, compared to those of all shear-thinning models. Although instantaneous WSS distributions, and λ_{ci} and $\overline{\lambda_{ci}}$ contours agree that the Newtonian model is applicable for the regions with $|\dot{\gamma}| > 50\ \mathrm{s}^{-1}$, in Fig. 9, there are significant differences in OSI and ECAP distributions between the Newtonian and shear-thinning models, especially for Case 2, which has the highest mean flow rate. Supplementary Video-2 presents the temporal evolution of $|\dot{\gamma}|$ distribution inside the bulge for all three waveforms. Together with the vortex structure, a larger $|\dot{\gamma}|$ region is also transported through the bulge. Although Case 1 could not obtain a large $|\dot{\gamma}|$ through the aneurysm, the transport of vortex pattern is slow, eliminating the long stagnation at specified sections inside the bulge. However, for Case 2, the transport of vortex pattern is accomplished within a very short time, leading to a highly stagnant flow structure at the proximal and central regions. In those highly stagnant regions, the Newtonian predicts an OSI_{max} twice as large as that predicted by the Carreau and Power models, along with an ECAP_{max} that is 5 times greater. Therefore, within the aneurysm bulge, in addition to $|\dot{\gamma}|$ distribution, the vortex transport mechanism (VTM) is also an important factor to consider when selecting a rheology model.

For the shear-thinning models, the Casson and Quemada models are closer to the Newtonian model than the Carreau and Power models for $|\dot{\gamma}| < 100\ \mathrm{s}^{-1}$, and they exhibit diverging behavior from the Newtonian model at high $|\dot{\gamma}|$, which is not expected. However, according to Fig. 10, the difference between the viscoelastic and Newtonian models is relatively small compared to that between the shear-thinning models even at low $|\bar{\dot{\gamma}}|$, which is consistent with the findings of (Bodnár et al., 2011).

CONCLUSIONS

The study yields the following conclusions:

- The IFW pattern has a significant impact on VTM,
- The strength of the vortices and their transportation mechanism (VTM) both influence the distribution and magnitude of the TAWSS, OSI, ECAP, and RRT,
- The vortex transport mechanism (VTM) is also an important factor to consider when selecting a rheology model because high $|\dot{\gamma}|$ region is also transported with VTM,
- The effect of elastic behavior is relatively minor compared to the effect of viscous shear-thinning behavior,
- Even at high flow rates, the Newtonian model is not appropriate for modeling AAA hemodynamics. Rather than the Newtonian model, the Carreau and Power models, together with proper patient-specific constants, are more stable than Casson and Quemada, and recommended (Saqr et al., 2020).

This study, as a comparative parametric analysis, is subject to several limitations that could influence the obtained results. The idealization of aneurysm bulge rather than utilizing patient-specific geometry may lead to inadequate simulation of the exact aneurysm hemodynamics, together with omitting the wall compliance and Windkessel boundary conditions. Therefore, future studies will aim to incorporate patient-specific geometries with elastic walls, Windkessel boundary conditions, along with implementing the Oldroyd-B model for high Reynolds number. Finally, VTM can be observed by applying a turbulence model such as LES.

REFERENCES

Arzani, A. (2016). Hemodynamics and transport in patient-specific abdominal aortic aneurysms (Doctoral dissertation, University of California, Berkeley).

Arzani, A. (2018). Accounting for residence-time in blood rheology models: Do we really need non-Newtonian blood flow modelling in large arteries? Journal of the Royal Society Interface, 15(146). https://doi.org/10.1098/rsif.2018.0486

Arzani, A., & Shadden, S. C. (2016). Characterizations and correlations of wall shear stress in aneurysmal flow. Journal of Biomechanical Engineering, 138(1). https://doi.org/10.1115/1.4032056

Bessonov, N., Simakov, A. S. S., Vassilevskii, Y., & Volpert, V. (2016). Methods of blood flow modelling. Mathematical Modelling of Natural Phenomena, 11(1), 1–25. https://doi.org/10.1051/mmnp/201611101

Biasetti, J., Hussain, F., & Gasser, T. C. (2011). Blood flow and coherent vortices in the normal and aneurysmatic aortas: A fluid dynamical approach to intraluminal thrombus formation. Journal of the Royal Society Interface, 8(63), 1449–1461. https://doi.org/10.1098/rsif.2011.0041

Bilgi, C., & Atalik, K. (2019). Numerical investigation of the effects of blood rheology and wall elasticity in abdominal aortic aneurysm under pulsatile flow conditions. Biorheology, 56(1), 51–71. https://doi.org/10.3233/BIR-180202

Bilgi, C., & Atalık, K. (2020). Effects of blood viscoelasticity on pulsatile hemodynamics in arterial aneurysms. Journal of Non-Newtonian Fluid Mechanics, 279, Article 104263. https://doi.org/10.1016/j.jnnfm.2020.104263

Bodnár, T., Sequeira, A., & Prosi, M. (2011). On the shear-thinning and viscoelastic effects of blood flow under various flow rates. Applied Mathematics and Computation, 217(11), 5055–5067. https://doi.org/10.1016/j.amc.2010.07.054

Brewster, D. C., Cronenwett, J. L., Hallett, J. W., Johnston, K. W., Krupski, W. C., & Matsumura, J. S. (2003). Guidelines for the treatment of abdominal aortic aneurysms: Report of a subcommittee of the Joint Council of the American Association for Vascular Surgery and Society for Vascular Surgery. Journal of Vascular Surgery, 37(5), 1106–1117. https://doi.org/10.1067/mva.2003.363

Chen, Q., Zhong, Q., Qi, M., & Wang, X. (2015). Comparison of vortex identification criteria for planar velocity fields in wall turbulence. Physics of Fluids, 27(8). https://doi.org/10.1063/1.4927647

Cho, Y. I., & Kensey, K. R. (1991). Effects of the non-Newtonian viscosity of blood on flows in a diseased arterial vessel. Part 1: Steady flows. Biorheology, 28(3–4), 241–262. https://doi.org/10.3233/BIR-1991-283-415

Deplano, V., Guivier-Curien, C., & Bertrand, E. (2016). 3D analysis of vortical structures in an abdominal aortic aneurysm by stereoscopic PIV. Experiments in Fluids, 57(11), 167. https://doi.org/10.1007/s00348-016-2263-0

Egelhoff, C. J., Budwig, R. S., Elger, D. F., Khraishi, T. A., & Johansen, K. H. (1999). Model studies of the flow in abdominal aortic aneurysms during resting and exercise conditions. Journal of Biomechanics, 32(12), 1319–1329. https://doi.org/10.1016/S0021-9290(99)00134-7

Elhanafy, A., Guaily, A., & Elsaid, A. (2019). Numerical simulation of Oldroyd-B fluid with application to hemodynamics. Advances in Mechanical Engineering, 11(5), 1–7. https://doi.org/10.1177/1687814019852844

Epps, B. P. (2017). Review of vortex identification methods. AIAA SciTech Forum - 55th AIAA Aerospace Sciences Meeting, 1–22. https://doi.org/10.2514/6.2017-0989

Faraji, A., Sahebi, M., & Salavati Dezfouli, S. (2022). Numerical investigation of different viscosity models on pulsatile blood flow of thoracic aortic aneurysm (TAA) in a patient-specific model. Computer Methods in Biomechanics and Biomedical Engineering, 0(0), 1–13. https://doi.org/10.1080/10255842.2022.2102423

Favero, J. L., Secchi, A. R., Cardozo, N. S. M., & Jasak, H. (2010). Viscoelastic flow analysis using the software OpenFOAM and differential constitutive equations. Journal of Non-Newtonian Fluid Mechanics, 165(23–24), 1625–1636. https://doi.org/10.1016/j.jnnfm.2010.08.010

Finol, E. A., & Amon, C. H. (2001). Blood flow in abdominal aortic aneurysms: Pulsatile flow hemodynamics. Journal of Biomechanical Engineering, 123(5), 474–484. https://doi.org/10.1115/1.1395573

Fisher, C., & Rossmann, J. S. (2009). Effect of non-Newtonian behavior on hemodynamics of cerebral aneurysms. Journal of Biomechanical Engineering, 131(9), 1–9. https://doi.org/10.1115/1.3148470

Fuchs, A., Berg, N., & Prahl Wittberg, L. (2021). Pulsatile aortic blood flow—A critical assessment of boundary conditions. ASME Journal of Medical Diagnostics, 4(1), 011002. https://doi.org/10.1115/1.4048978

Guranov, I., Ćoćić, A., & Lečić, M. (2013). Numerical studies of viscoelastic flow using the software OpenFOAM. Proceedings in Applied Mathematics and Mechanics, 13(1), 591–592. https://doi.org/10.1002/pamm.201310276

Habla, F., Tan, M. W., Haßlberger, J., & Hinrichsen, O. (2014). Numerical simulation of the viscoelastic flow in a three-dimensional lid-driven cavity using the log-conformation reformulation in OpenFOAM. Journal of Non-Newtonian Fluid Mechanics, 212, 47–62. https://doi.org/10.1016/j.jnnfm.2014.08.005

Javidi, M., & Hrymak, A. N. (2015). Numerical simulation of the dip-coating process with wall effects on the coating film thickness. Journal of Coatings Technology and Research, 12(5), 843–853. https://doi.org/10.1007/s11998-015-9699-7

Juster, H. R., Distlbacher, T., & Steinbichler, G. (2014). Viscosity analysis of a polymer-based drug delivery system using open-source CFD methods and high-pressure capillary rheometry. International Polymer Processing, 29(5), 570–578. https://doi.org/10.3139/217.2892

Karimi, S., Dabagh, M., Vasava, P., Dadvar, M., Dabir, B., & Jalali, P. (2014). Effect of rheological models on the hemodynamics within human aorta: CFD study on CT image-based geometry. Journal of Non-Newtonian Fluid Mechanics, 207, 42–52. https://doi.org/10.1016/j.jnnfm.2014.03.007

Lee, S. W., & Steinman, D. A. (2007). On the relative importance of rheology for image-based CFD models of the carotid bifurcation. Journal of Biomechanical Engineering, 129(2), 273–278. https://doi.org/10.1115/1.2540836

Les, A. S., Shadden, S. C., Figueroa, C. A., Park, J. M., Tedesco, M. M., Herfkens, R. J., Dalman, R. L., & Taylor, C. A. (2010). Quantification of hemodynamics in abdominal aortic aneurysms during rest and exercise using magnetic resonance imaging and computational fluid dynamics. Annals of Biomedical Engineering, 38(4), 1288–1313. https://doi.org/10.1007/s10439-010-9949-x

Leuprecht, A., & Perktold, K. (2001). Computer simulation of non-Newtonian effects on blood flow in large arteries. Computer Methods in Biomechanics and Biomedical Engineering, 4(2), 149–163. https://doi.org/10.1080/10255840008908002

Maazioui, S., Kissami, I., Benkhaldoun, F., Maazouz, A., & Ouazar, D. (2021). Concentrated phosphate slurry flow simulations using OpenFOAM. Proceedings of the International Conference on Industrial Engineering and Operations Management, 1843–1852.

Madhavan, S., & Kemmerling, E. M. C. (2018). The effect of inlet and outlet boundary conditions in image-based CFD modeling of aortic flow. Biomedical Engineering Online, 17(1), 1–21. https://doi.org/10.1186/s12938-018-0497-1

McGloughlin, T. M., & Doyle, B. J. (2010). New approaches to abdominal aortic aneurysm rupture risk assessment. Arteriosclerosis, Thrombosis, and Vascular Biology, 30(9), 1687–1694. https://doi.org/10.1161/ATVBAHA.110.204529

Mendieta, J. B., Fontanarosa, D., Wang, J., Paritala, P. K., McGahan, T., Lloyd, T., & Li, Z. (2020). The importance of blood rheology in patient-specific computational fluid dynamics simulation of stenotic carotid arteries. Biomechanics and Modeling in Mechanobiology, 19(5), 1477–1490. https://doi.org/10.1007/s10237-019-01282-7

Morbiducci, U., Gallo, D., Massai, D., Ponzini, R., Deriu, M. A., Antiga, L., Redaelli, A., & Montevecchi, F. M. (2011). On the importance of blood rheology for bulk flow in hemodynamic models of the carotid bifurcation. Journal of Biomechanics, 44(13), 2427–2438. https://doi.org/10.1016/j.jbiomech.2011.06.028

Moyle, K. R., Antaki, J. F., Greenwald, L., Hariharan, P., & Reddy, V. M. (2006). Comparison of inflow boundary conditions for hemodynamic simulations in idealized and anatomically realistic models of the aorta. Journal of Biomechanical Engineering, 128(5), 745–749. https://doi.org/10.1115/1.2187035

Mutlu, O., Salman, H. E., Al-Thani, H., El-Menyar, A., Qidwai, U. A., & Yalcin, H. C. (2023). How does hemodynamics affect rupture tissue mechanics in abdominal aortic aneurysm: Focus on wall shear stress derived parameters, time-averaged wall shear stress, oscillatory shear index, endothelial cell activation potential, and relative residence time. Computers in Biology and Medicine, 154. https://doi.org/10.1016/j.compbiomed.2023.106609

Ohtaroglu, O. (2020). Experimental investigation of physiological flow in abdominal aortic aneurysm (Master's thesis, Middle East Technical University, Ankara, Turkey).

Pinto, S. I. S., & Campos, J. B. L. M. (2016). Numerical study of wall shear stress-based descriptors in the human left coronary artery. Computer Methods in Biomechanics and Biomedical Engineering, 19(13), 1443–1455. https://doi.org/10.1080/10255842.2016.1149575

Qiu, Y., Yuan, D., Wen, J., Fan, Y., & Zheng, T. (2018). Numerical identification of the rupture locations in patient-specific abdominal aortic aneurysms using hemodynamic parameters. Computer Methods in Biomechanics and Biomedical Engineering, 21(1), 1–12. https://doi.org/10.1080/10255842.2017.1410796

Quemada, D. (1978). Rheology of concentrated disperse systems. Rheologica Acta, 653, 643–653.

Ramazanli, B., Yavuz, M. M., & Sert, C. (2023). Effect of inlet velocity profile and entrance length on abdominal aortic aneurysm hemodynamics simulations. Journal of Thermal Science and Technology, 43(2), 159–174. https://doi.org/10.47480/isibted.1391391

Razavi, A., Shirani, E., & Sadeghi, M. R. (2011). Numerical simulation of blood pulsatile flow in a stenosed carotid artery using different rheological models. Journal of Biomechanics, 44(11), 2021–2030. https://doi.org/10.1016/j.jbiomech.2011.04.023

Reza, M. M. S., & Arzani, A. (2019). A critical comparison of different residence time measures in aneurysms. Journal of Biomechanics, 88, 122–129. https://doi.org/10.1016/j.jbiomech.2019.03.028

Saha, S. C., Francis, I., Saha, G., Huang, X., & Molla, M. M. (2024). Hemodynamic Insights into Abdominal Aortic Aneurysms: Bridging the Knowledge Gap for Improved Patient Care. Fluids, 9(2), 50. https://doi.org/10.3390/fluids9020050

Salman, H. E., Ramazanli, B., Yavuz, M. M., & Yalcin, H. C. (2019). Biomechanical investigation of disturbed hemodynamics-induced tissue degeneration in abdominal aortic aneurysms using computational and experimental techniques. Frontiers in Bioengineering and Biotechnology, 7, Article 111. https://doi.org/10.3389/fbioe.2019.00111

Saqr, K. M., Rashad, S., Tupin, S., Niizuma, K., Hassan, T., Tominaga, T., & Ohta, M. (2020). What does computational fluid dynamics tell us about intracranial aneurysms? A meta-analysis and critical review. Journal of Cerebral Blood Flow & Metabolism, 40(5), 1021–1039. https://doi.org/10.1177/0271678X19854640

Scotti, C. M., Jimenez, J., Muluk, S. C., & Finol, E. A. (2008). Wall stress and flow dynamics in abdominal aortic aneurysms: Finite element analysis vs. fluid-structure interaction. Computer Methods in Biomechanics and Biomedical Engineering, 11(3), 301–322. https://doi.org/10.1080/10255840701827412

Soudah, E., Loong, E. Y. K., Bordone, T. H., Pua, M., & Narayanan, S. (2013). CFD modelling of abdominal aortic aneurysm on hemodynamic loads using a realistic geometry with CT. Computational and Mathematical Methods in Medicine, 2013, Article 472564. https://doi.org/10.1155/2013/472564

Soulis, J. V., Giannoglou, G. D., Chatzizisis, Y. S., Seralidou, K. V., Parcharidis, G. E., & Louridas, G. E. (2008). Non-Newtonian models for molecular viscosity and wall shear stress in a 3D reconstructed human left coronary artery. Medical Engineering & Physics, 30(1), 9–19. https://doi.org/10.1016/j.medengphy.2007.02.001

Stamatopoulos, C., Papaharilaou, Y., Mathioulakis, D. S., & Katsamouris, A. (2010). Steady and unsteady flow within an axisymmetric tube dilatation. Experimental Thermal and Fluid Science, 34(7), 915–927. https://doi.org/10.1016/j.expthermflusci.2010.02.008

Stergiou, Y. G., Athanasios, G. K., Aikaterini, A. M., & Spiros, V. P. (2019). Fluid-Structure Interaction in Abdominal Aortic Aneurysms: Effect of Haematocrit. Fluids, 4(1), 11. https://doi.org/10.3390/fluids4010011

Suh, G.-Y., Les, A. S., Tenforde, A. S., Shadden, S. C., Spilker, R. L., Yeung, J. J., Cheng, C. P., Herfkens, R. J., Dalman, R. L., & Taylor, C. A. (2011). Hemodynamic Changes Quantified in Abdominal Aortic Aneurysms with Increasing Exercise Intensity Using MR Exercise Imaging and Image-Based Computational Fluid Dynamics. Annals of Biomedical Engineering, 39(2), 864–883. https://doi.org/10.1007/s10439-011-0313-6

Wei, Z. A., Huddleston, C., Trusty, P. M., Singh-Gryzbon, S., Fogel, M. A., Veneziani, A., & Yoganathan, A. P. (2019). Analysis of inlet velocity profiles in numerical assessment of Fontan hemodynamics. Annals of Biomedical Engineering, 47(11), 2258–2270. https://doi.org/10.1007/s10439-019-02307-z

Weller, H. G., Tabor, G., Jasak, H., & Fureby, C. (1998). A tensorial approach to computational continuum mechanics using object-oriented techniques. Computers in Physics, 12(6), 620. https://doi.org/10.1063/1.168744

Womersley, J. R. (1955). Method for the calculation of velocity, rate of flow, and viscous drag in arteries when the pressure gradient is known. The Journal of Physiology, 127(3), 553–563. https://doi.org/10.1113/jphysiol.1955.sp005276

Zheng, E. Z., Rudman, M., Singh, J., & Kuang, S. B. (2019). Direct numerical simulation of turbulent non-Newtonian flow using OpenFOAM. Applied Mathematical Modelling, 72, 50–67. https://doi.org/10.1016/j.apm.2019.03.003